ACS APPLIED MATERIALS & INTERFACES

www.acsami.org

Research Article

Physically Unclonable Surfaces Enabled by Cold Spray Deposition

Jaehun Jeon and Semih Akin*

Cite This: https://doi.org/10.1021/acsami.5c17570

Read Online

ACCESS | Metrics & More | Article Recommendations | Supporting Information

ABSTRACT: As counterfeit components become increasingly prevalent, encoded surfaces, particularly physically unclonable functions (PUFs), have emerged as powerful tools for secure part authentication and reliable traceability. However, significant challenges remain in fabricating unclonable surface structures in a high-throughput, scalable, and cost-effective manner while also ensuring robust encryption and secure authentication. This work aims to address the existence gaps by introducing an innovative approach to PUF manufacturing utilizing the cold spray (CS) particle deposition technique, complemented by algorithmic feature extraction and cryptographic surface encoding. In our approach, a mixture of metal and fluorescent microparticles is deposited onto an aluminum (Al 5052) substrate by leveraging the process-specific two-phase (gas−solid) turbulent flow characteristic of the CS process. The inherent stochasticity of the CS flow leads to a random distribution of fluorescent particles, generating unique, physically unclonable luminescent patterns on the target surface. The spatial distribution of the optical fluorescent particles is then captured under UV light (365 nm) exposure and subsequently processed through image binarization. Features are extracted from this distribution by using Voronoi analysis. The extracted features are then encrypted using the SHA-256 cryptographic algorithm to generate a secure "certification key" for part authentication. Experimental results demonstrate the effectiveness of the proposed manufacturing approach for high-throughput, scalable PUF production, confirming its suitability for robust part authentication and its reliability under environmental stressors (e.g., thermal cycling, chemical exposure). The developed method shows strong potential for enabling tamper-evident part authentication solutions to address the growing threat of counterfeiting in critical sectors, such as aerospace, defense, and advanced manufacturing.

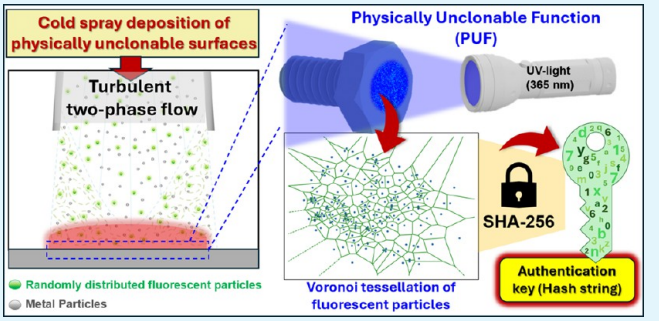

KEYWORDS: *physical unclonable surfaces, physical unclonable function (PUF), cold spray, additive manufacturing, Voronoi analysis, encryption, part authentication, SHA-256*

1. INTRODUCTION

With the advent of fourth industrial revolution, which integrates digital manufacturing with intelligent data-driven systems,[1] part authentication has become increasingly vital for ensuring product integrity and security. Counterfeit parts pose significant threats to society as they can undermine safety, reduce performance, and compromise trust across critical sectors (e.g., aerospace,[2] automotive, defense,[3] electronics,[4] healthcare,[5] and textiles[6]). Historically, multiple catastrophic incidents[5,7−9] have been directly linked to counterfeit parts, resulting in casualties and safety failures. Beyond these incidents, the OECD's 2025 report on global trade in fake goods[10] estimates that counterfeit parts account for more than $467 billion in annual economic loss,[10] with automotive parts, pharmaceuticals, and electronics posing the greatest risks to consumer health and safety.[10,11] These realities underscore the urgent need for robust, tamper-resistant authentication strategies to safeguard product integrity, protect consumer safety, and secure supply chains against counterfeit infiltration.

At present, industries rely on serial numbers,[12] QR codes,[13] and watermarks[14] for product identification across supply chains. However, these traditional approaches are easily replicated and prone to degradation under environmental stressors.[14] Although RFID tags have gained traction in recent decades,[15−18] they remain susceptible to cloning, tampering, and signal interception, which limit their effectiveness as standalone solutions. Embedding identifiers (e.g., RFID,[19] QR codes[20]) into critical parts can improve traceability and enable part-level tracking.[6,15] However, these approaches require dedicated fabrication processes that compromise cost efficiency and scalability while also introducing stress concentrators that weaken mechanical performance. Collectively, these limitations underscore the need for advanced manufacturing techniques and tamper-resistant authentication strategies to effectively combat counterfeiting.

Received: September 3, 2025
Revised: December 18, 2025
Accepted: January 21, 2026

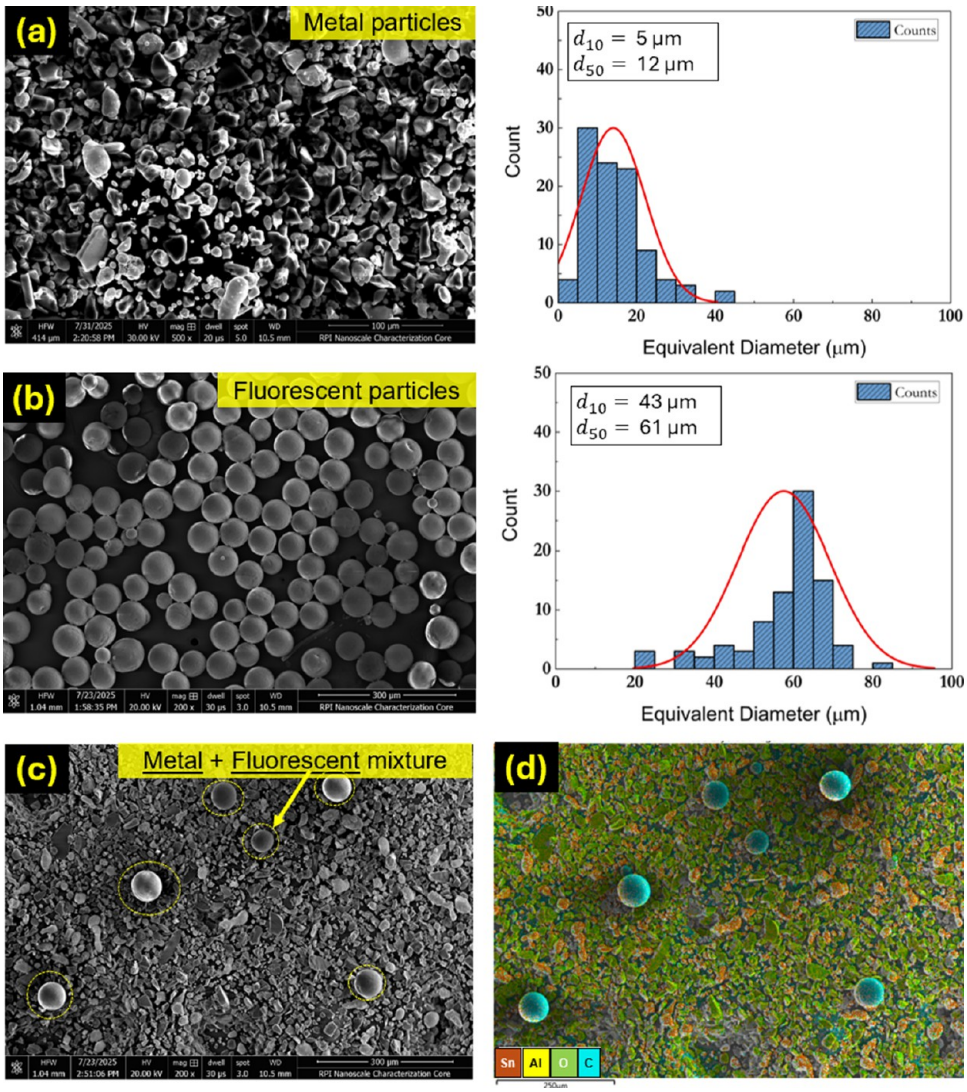

Figure 1. Morphology of the feedstock powders: (a) Metal (Al_2O_3 + Sn) powders; (b) fluorescent powders with corresponding size distribution; (c) microstructure of the metal–fluorescent powder blend for cold spraying; (d) corresponding EDX map.

In this context, recent research has focused on innovative authentication strategies based on physical unclonable functions (PUFs).[21−23] PUFs exploit inherent stochastic physical patterns as unique, unclonable digital identifiers, offering a robust means to prevent counterfeiting and mitigate cyber-related threats.[24,25] In essence, PUFs are created by harnessing the process-inherent stochasticity to fabricate physically unclonable surfaces,[26] which are then digitized through a set of feature extraction and encoding methods.[27] In this context, the scalable and high-throughput fabrication of unclonable surfaces, followed by efficient surface digitization and encryption is critical for enabling practical deployment of PUFs across mission-critical sectors.

Recent efforts in PUF fabrication have explored diverse approaches, including electronic circuit variability,[28] optical and photonic scattering patterns,[6,24,26,29] acoustic signatures,[29] magnetic domain randomness,[30] and coating-based surface patterns,[26,31] each exploiting inherent stochasticity to create unique, unclonable identifiers. Among these, coating-based surface PUFs have gained particular attention for their compatibility with structural components, enabling part-level authentication and traceability without significantly altering the geometry or functionality.[26,31,32] Various deposition techniques have been explored for fabricating PUFs, including spin-coating,[26,33,34] electrospraying,[32] and inkjet printing.[35] Despite this progress, challenges remain in achieving scalable, cost-effective, and high-throughput fabrication, as well as ensuring robust encoding and reliable authentication.

This work aims to address existing gaps in this emerging field by introducing an innovative PUF manufacturing approach based on cold spray (CS) particle deposition of fluorescent particles. While recent studies[33,36,37] have demonstrated the successful realization of PUFs by employing fluorescent materials as optical markers to generate PUFs, most of these approaches rely on complex, multistep fabrication or surface patterning techniques. Unlike conventional methods, our approach exploits the inherent stochasticity of CS deposition of optical markers (i.e., a powder blend of metal powders and fluorescent additives) to directly generate unclonable surfaces in a single step.

The inherent randomness of the CS process—arising from the turbulent two-phase (gas–solid) flow—generates a stochastic distribution of fluorescent particles with strong adhesion, thereby creating distinctive and irreproducible

https://doi.org/10.1021/acsami.5c17570
ACS Appl. Mater. Interfaces XXXX, XXX, XXX−XXX

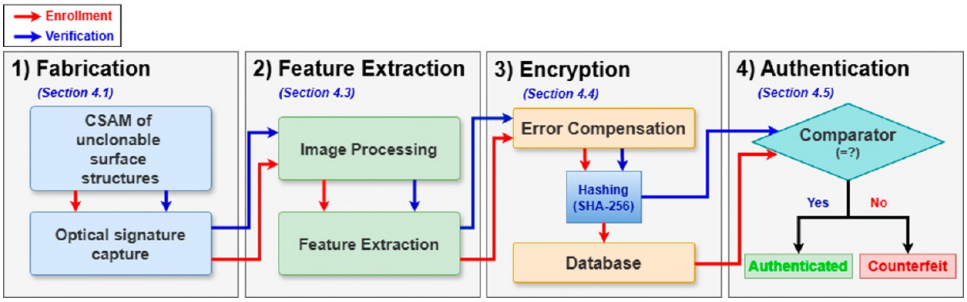

Figure 2. Flowchart of the overall process steps: Red arrows indicate the surface enrollment process, and blue arrows represent the verification (authentication) pipeline of the fabricated surfaces.

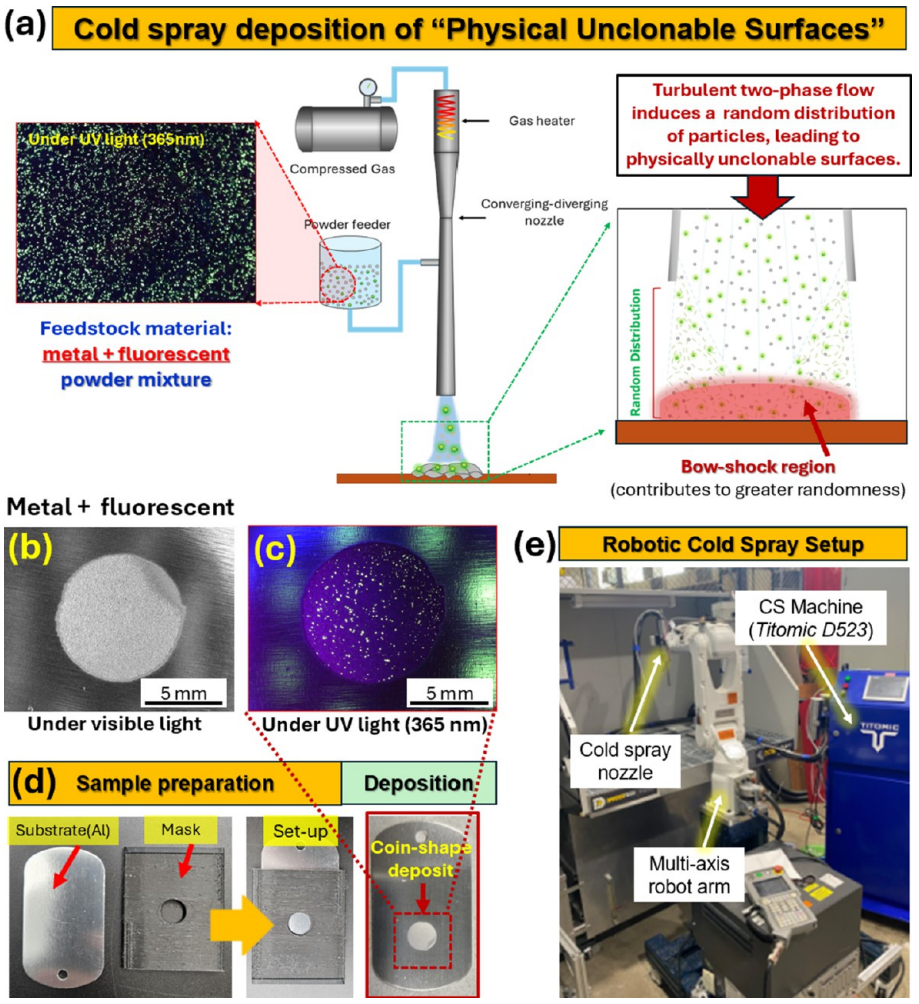

Figure 3. Additively manufactured unclonable surfaces: (a) Schematic illustrating CS deposition of unique, random surface structures. CS-deposited (metal + fluorescent) surfaces (b) under visible light and (c) under UV light. (d) Sample preparation and surface deposition on an aluminum substrate. (e) Robotic cold spray setup.

patterns. Unique features are then algorithmically extracted from the spatial arrangement of the fluorescent particles under UV light illumination and secured by cryptographic surface encoding. To demonstrate practical utility, a case study on part authentication is conducted using a service-grade structural bolt. Overall, this study advances the field by introducing the following key innovations:

i. A novel physically unclonable surface manufacturing pathway achieved by cold spraying of fluorescent additives as hidden optical patterns (signatures).
ii. An end-to-end surface encryption and authentication framework that integrates feature extraction, surface encoding, and cryptographic validation to ensure secure, tamper-resistant, and scalable part authentication.
iii. Demonstration of the proposed framework for robust part-level authentication across structural components, validating real-world applicability.

The remainder of this work is organized as follows: Section 2 presents the materials. Section 3 and Section 4 details the methods, including surface fabrication, feature extraction,

https://doi.org/10.1021/acsami.5c17570
ACS Appl. Mater. Interfaces XXXX, XXX, XXX−XXX

surface uniqueness evaluation, surface encryption, and authentication. Section 5 provides a part-level authentication case study. Finally, Sections 6 and 7 present the discussions and concluding remarks.

2. MATERIALS

An aluminum alloy (*Al 5052*) plate was used as the target substrate for the CS process. The feedstock powders comprise a tailored blend of micrometer-scale metal powders and polymer-based fluorescent powders. The metallic powder content (*LPP.T-25, Titomic Inc., USA*) consists of tin (Sn, 50 wt %) and aluminum oxide (Al_2O_3, 50 wt %). In this mixture, Sn imparts sufficient ductility to promote metallurgical bonding with the target surface,[38] while the oxide content enhances wear resistance, thermal stability, and mechanical integrity of the deposited coating.[39] The fluorescent polyethylene microspheres (*UVYGPMS-0.97, Cospheric Inc., USA*) were incorporated into the blend as optical markers for PUF generation. These microspheres are composed of transparent low-density polyethylene (ρ = 0.98 g cm^{-3}) with fluorophores embedded within the polymer matrix, exhibiting a yellow-green fluorescence (561 nm) under 365 nm UV illumination.[40]

The morphology and size distribution of the constituent metallic and fluorescent feedstock particles were acquired by scanning electron microscopy (SEM, *FEI Versa*) and are shown in Figure 1a,b. The particle size distribution was determined using image editing software (*ImageJ*), revealing mean diameters of d_{50} = 12 μm for the metallic particles and d_{50} = 61 μm for the fluorescent particles. To prepare the feedstock for cold spraying, the powders were gently blended at 99 wt % metallic and 1 wt % fluorescent to minimize particle breakage and morphological changes. Figure 1c shows the microstructure of the resulting blend prior to cold spraying. The energy-dispersive X-ray spectroscopy (EDX) map in Figure 1d confirms the distribution of both metallic and fluorescent particles within the blend.

3. METHODS

This section describes the methods for fabricating PUFs, together with the associated encryption and authentication framework, as illustrated in Figure 2 (i.e., red arrows indicate encryption and enrollment, while blue arrows denote surface authentication/verification). The proposed pipeline proceeds sequentially through (1) CS deposition of randomized, high-entropy optical patterns, along with surface uniqueness verification, (2) feature extraction from the fabricated surface, (3) encryption of the extracted features, and (4) surface authentication. A step-by-step breakdown of each stage is provided in the following subsections.

4. RESULTS AND DISCUSSION

4.1. Fabrication of Physically Unclonable Surfaces

To fabricate randomly distributed surface patterns, the CS particle deposition technique was employed. CS is an emerging solid-state additive manufacturing technique[41,42] that propels metallic powders at supersonic speeds using a high-pressure gas stream through a converging-diverging nozzle (see Figure 3a). The inherently turbulent gas-particle flow in the CS process promotes stochastic particle deposition, leading to a random pattern formation on the substrate. In addition, the bow shock formed near the substrate by the supersonic particle−gas jet[43−45] intensifies the randomness of particle distribution, as illustrated in Figure 3a (right panel). Overall, CS enables high-throughput and scalable fabrication of physically unclonable surfaces through its process-specific turbulent, supersonic two-phase flow regime.

Despite these advantages of CS, achieving a sparsely dispersed particle distribution on the surface remains challenging due to particle agglomeration and difficulties in controlling deposition parameters and flow dynamics. As shown in Figure 3b, dense particle deposition may complicate feature extraction as overlapping clusters can obscure spatial patterns critical for accurate characterization and authentication. These factors hinder the generation of reliable digital fingerprints (PUFs) by increasing processing complexity and reducing pattern randomness. While pulsed-CS methods[46−48] can improve control over particle density and distribution, they still face issues of equipment complexity and limited scalability for large areas. As such, alternative or complementary approaches are needed to preserve high pattern uniqueness while enhancing the process efficiency and scalability.

To this end, we incorporate a low concentration (1 wt %) of fluorescent powder additives into the conventional metal powder feedstock in CS, aiming to achieve highly randomized distribution of sparsely dispersed optical markers on the target substrate. In parallel, the high metallic content (> 99 wt %) in the mixture facilitates the entrapment of fluorescent particles and ensures their effective deposition on the surface with strong adhesion. Furthermore, the inclusion of fluorescent powders enhances unclonability and mitigates potential security risks by providing a hidden optical fingerprint that is difficult to detect under visible light. As such, this dual functionality significantly strengthens the overall security and reliability of the fabricated surfaces.

Building on this innovation, unclonable surfaces were fabricated, as shown in Figure 3c. To produce coin-shaped deposits, a shadow mask was employed (Figure 3d). The deposition was performed using a low-pressure cold spray system (*Titomic D523*) as shown in Figure 3e, in which the deposition nozzle was mounted on a multiaxis robotic arm (*Yaskawa*) for precise process control. Compressed air was used as the propelling gas with a stagnation temperature of 100 °C and a stagnation pressure of 0.6 MPa. The spray distance was set to 15 mm, and the nozzle transverse speed was 150 mm/s. Under these settings, unclonable surface deposition was achieved in a high-throughput manner, requiring only 3 s to complete a single surface deposition (Video S1, Supporting Information). This rapid fabrication capability highlights the scalability of the CS process for PUF production.

Figure 4a,b shows the surface and cross-sectional microstructure of the resulting deposition, along with their elemental distribution. The surface microstructure reveals a well-consolidated material deposition with negligible porosity. Notably, the fluorescent particles exhibited noticeable plastic deformation upon impact and are firmly embedded within the metallic matrix, indicating strong mechanical interlocking and adhesion to the underlying substrate. Such deformation and secure entrapment are critical for ensuring surface durability and reliability under demanding conditions. Cross-sectional images in Figure 4b further confirm the continuous thin film formation on the substrate with negligible porosity, indicating a dense, well-bonded coating. Such microstructural integrity suggests strong interfacial adhesion, which is further validated through Scotch tape-based peel tests, where all fluorescent particles remained intact throughout the peeling cycles (see Video S2 and Figure S1, Supporting Information).

The EDX analysis confirmed the encapsulation of a plastically deformed fluorescent particle within the metallic matrix, as evidenced by the characteristic carbon peak inherent to polymers. Furthermore, the cross-sectional EDX mapping revealed a uniform distribution of key coating elements (i.e., C, Sn, and Al) across the material interface. Taken together, the microstructural analyses demonstrated that the coating exhibits

https://doi.org/10.1021/acsami.5c17570
ACS Appl. Mater. Interfaces XXXX, XXX, XXX−XXX

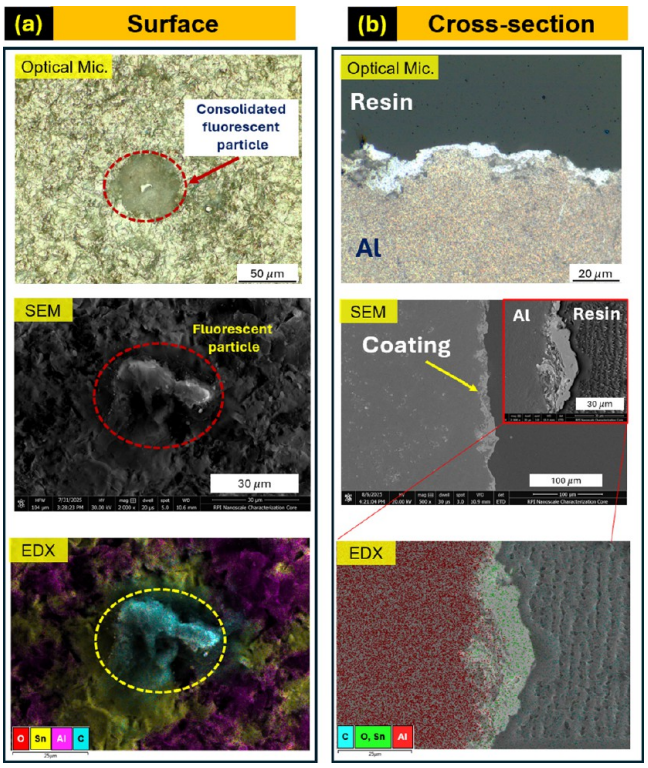

Figure 4. Microstructure of the fabricated coatings: (a) Surface microstructure; (b) cross-sectional microstructure obtained via optical microscopy (top panel) and SEM (middle panel), with corresponding EDX maps (bottom panel).

strong fluorescent particle entrapment and robust interfacial bonding, all of which are integral to ensuring long-term durability, mechanical stability, and reliable performance of the fabricated unclonable surfaces.

4.2. Surface Uniqueness Quantification and Analysis

In this section, to ensure the unclonability and robustness of the fabricated surfaces, systematic image processing and subsequent optical evaluations are performed based on the uniformity,[49] Hamming Distance, the intra-Hamming Distance (intra-HD), and inter-Hamming Distance (inter-HD)[50] analyses. Next, the cloning probability and NIST SP 800-22 statistical test[51] are applied to assess the randomness of the surfaces. Last, the fabricated surfaces (PUFs) were benchmarked against existing studies including a comparison of their fabrication processes. Detailed descriptions of each metric calculation are provided in the Supporting Information (Section 2).

4.2.1. Image Processing and Binarization. To digitize the resulting physical surface deposition, first, the spatial distribution of fluorescent particles was extracted through an image processing procedure. In this regard, first, images of the as-CS deposited surfaces (Figure 5a, left panel) were captured using a hand-held portable digital microscope (*KWHRYVRE*) under a collimated UV light source (*Alonefire*, 365 nm wavelength) positioned at a 45° angle to the substrate (see Figure 5a, right panel). All microscopic observations were conducted in a darkroom environment (without ambient light), and the fluorescent emission range was isolated through computational postprocessing. This imaging approach is affordable and straightforward and enables rapid, non-destructive image acquisition.

Following surface image acquisition, the coin-shaped region was cropped from the background using image editing software (*ImageJ*). Subsequently, the original BGR format images were converted to the HSV color space using a Python library (*OpenCV*) (Figure 5b, left panel). To clearly separate and highlight the fluorescent particles from the deposited metal matrix, a hue-channel mask in the yellow-green range was applied (hue values = 20−100 in the HSV color space), and image binarization was performed using global thresholding (Figure 5b, middle panel). Each particle region was subsequently segmented by its contour, and the centroid coordinates of fluorescent particles were recorded for further analysis (Figure 5b, right panel). This digital representation provides precise particle coordinates for quantitative analysis and feature extraction, which are essential for developing resilient PUFs.

Subsequently, to simplify the uniqueness metric evaluation, full-size binarized images were down-sampled. Each image was first transformed into a polar coordinate system (Figure 5c, left panel) and divided into 512 × 512 angular-radial regions. The pixel values within each regions were averaged using mean pooling (mean binning) to reconstruct a 512 × 512 pixel image. To preserve the essential features, the image was progressively down-sampled through successive mean pooling to resolutions of 256 × 256, 128 × 128, 64 × 64, and 32 × 32 pixels. From this 32 × 32 image, each 2 × 2 pixel block was converted into a single binary value based on a majority rule (if the number of nonzero pixels exceeds the number of zero pixels, the value is '1'). As shown in Figure 5c (right panel), this process yielded a compact binary image of 16 × 16 pixels, which was then flattened into a 256-bit binary vector (1, 256) for PUF metric evaluations described in the following section.

4.2.2. Surface Uniqueness Metrics and Statistical Validation. *4.2.2.1. Uniformity.* Initially, to validate the cryptographic robustness of the fabricated surfaces, uniformity was evaluated. This metric quantifies the balance between '1' and '0' bits in the binary sequence and is calculated as the proportion of '1' bits. For a reliable statistical assessment, 50 distinct unclonable surfaces were fabricated, and each response was binarized into a 256-bit code. As shown in Figure 6a, the resulting uniformity values exhibited a mean of 0.507 with a standard deviation of 0.042. These values are remarkably close to the ideal value of 0.5, indicating excellent randomness and an absence of bias between "0" and "1" bits, which is an essential attribute for authentication reliability of PUFs.[27]

4.2.2.2. Inter-HD, Intra-HD Metrics and Encoding Capacity. The uniqueness of the fabricated surfaces was evaluated using both inter-HD and intra-HD, which are statistical metrics quantifying the difference and similarity between binary sequences. First, as shown in Figure 6b, the inter-HD was calculated for the 50 different PUF responses previously used for uniformity evaluation, resulting in 1225 pairwise comparisons. The analysis yielded a mean inter-HD of 0.481 with a standard deviation of 0.044, confirming the strong uniqueness of the as-deposited surfaces with only a slight deviation from the ideal value of 0.5.[27,28,52] Detailed PUF responses for all 50 coin-shaped deposits are provided in the Supporting Information (see Figure S2a).

Subsequently, to assess the stability of the PUF responses, intra-HD analysis was conducted. The intra-HD represents the Hamming distance[27] between binary sequences obtained from repeated measurements of the same surface pattern. In this context, four distinct surfaces were selected, and 25 PUF

https://doi.org/10.1021/acsami.5c17570
ACS Appl. Mater. Interfaces XXXX, XXX, XXX−XXX

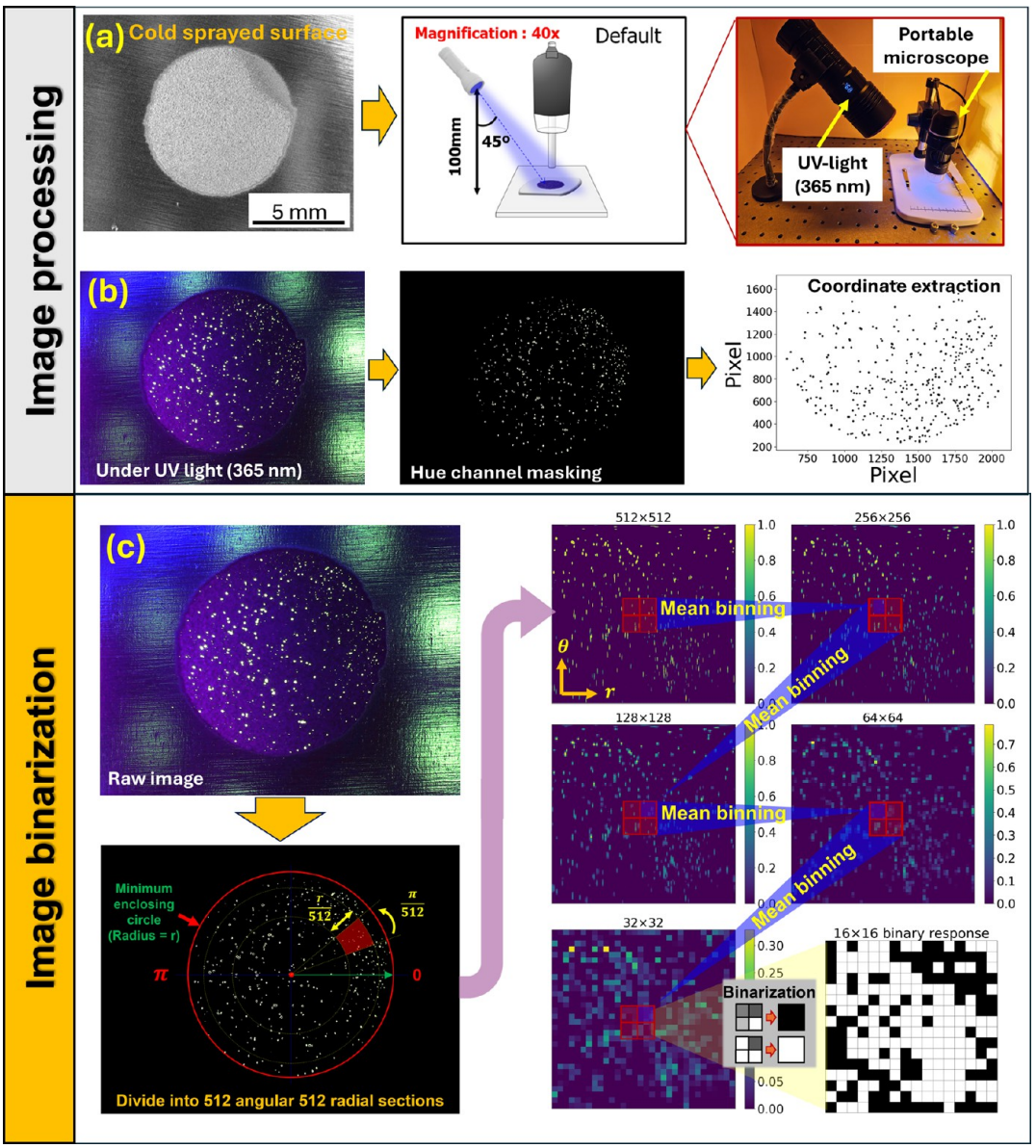

Figure 5. Image processing and binarization: (a,b) Digitization of the as-CS surface to capture the spatial distribution of fluorescent particles. (c) Image size-reduction methodology incorporating coordinate transformation, segmentation, and binarization.

responses were recorded for each. This resulted in a total of 1,200 pairwise comparisons across the four PUF groups (see Figure S2b, Supporting Information). The mean and standard deviation of the intra-HD values were 0.068 and 0.038, respectively, which are close to the ideal value of 0, demonstrating the high stability under repeated measurements.

Lastly, based on the inter-HD evaluation, effective number of independent bits (ENIB), also known as the degree of freedom,[27,53] was calculated (see Section 2.1, Supporting Information). The ENIB value quantifies the number of effective independent bits within the PUF responses.[27] The ENIB value was obtained as 128.95, corresponding to an available PUF capacity of $2^{128.95}$. This high ENIB value confirms the strong encoding capability and high entropy of the fabricated surfaces, thereby underscoring their suitability for security applications requiring large key spaces and robust uniqueness.

4.2.2.3. FPR and Cloning Probability. To statistically analyze the inter-HD and intra-HD distributions, normal distribution curves were fitted to the respective data sets. As shown in Figure 6c, the two fitted curves intersect at a specific point that defines the decision boundary between matching and nonmatching responses. The area of the inter-HD curve to the left of this intersection represents a false positive region. The ratio of this area to the total area under the inter-HD curve corresponds to the false positive rate (FPR).[27] The calculated FPR was 2.05×10^{-10}, indicating an extremely low probability of misauthentication with the PUF responses. Furthermore, the probability of cloning was determined by adding two areas (i.e., the false positive area and the false negative area). The false negative area, defined as the area under the intra-HD curve to the right of the intersection point, corresponds to genuine PUF responses that were incorrectly rejected. Based on the probability results in Figure 6c (right panel), the overall cloning probability was found to be 4.73×10^{-7}, confirming the resilience of the fabricated surfaces against unauthorized replication and highlighting their robustness for high-security authentication applications. Besides, the

https://doi.org/10.1021/acsami.5c17570
ACS Appl. Mater. Interfaces XXXX, XXX, XXX−XXX

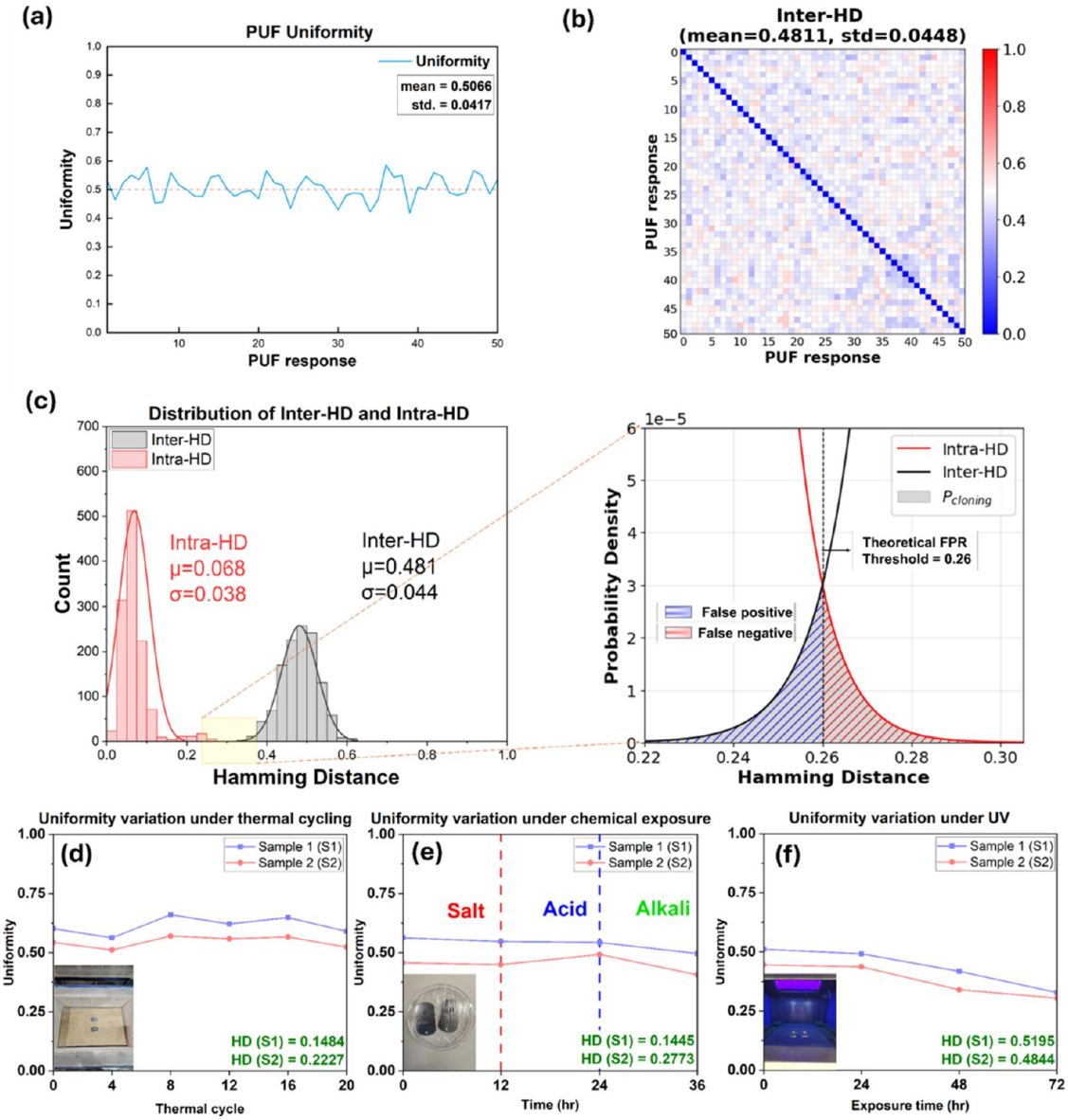

Figure 6. Evaluation of surface uniqueness and environmental durability: (a) Uniformity. (b) Inter-HD analysis. (c) Normal distribution fitting of intra-HD and inter-HD values illustrating their statistical separation. Durability analysis under (d) thermal cycling, (e) chemical exposure, and (f) high-density UV exposure.

Table 1. Benchmarking of PUF Studies

category	uniformity	intra-HD	inter-HD	process complexity	cost	year published	reference
optical PUFs	0.507	0.068	0.481	1 (single) step	low	this work	this work
	0.535	N/A	0.470	4 steps	medium	2021	26
	0.495	0.090	0.497	2 steps	medium	2025	29
	0.533	0.002	0.495	1 (single) step	low	2022	32
	0.503	N/A	0.490	4 steps	medium	2022	33
	0.500	0.120	0.500	3 steps	medium	2024	34
	0.498	0.068	0.500	3 steps	medium	2024	54
	0.493	0.082	0.491	3 steps	medium	2023	55
electronic PUFs	0.500	0	0.500	full foundry process	high	2025	28
	0.501	0	0.501	full foundry process	high	2025	52

NIST randomness test (i.e., NIST-800-22 evaluation)[51] verified the statistical randomness of the generated PUFs (see Section S2.2 and Table S1 in the Supporting Information).

4.2.2.4. Benchmarking of PUF Performance and Fabrication Process. Building on the uniqueness evaluation, the fabricated PUFs in this work were benchmarked against existing studies, including a comparison of their fabrication processes. Table 1 presents a summary of key performance

https://doi.org/10.1021/acsami.5c17570
ACS Appl. Mater. Interfaces XXXX, XXX, XXX−XXX

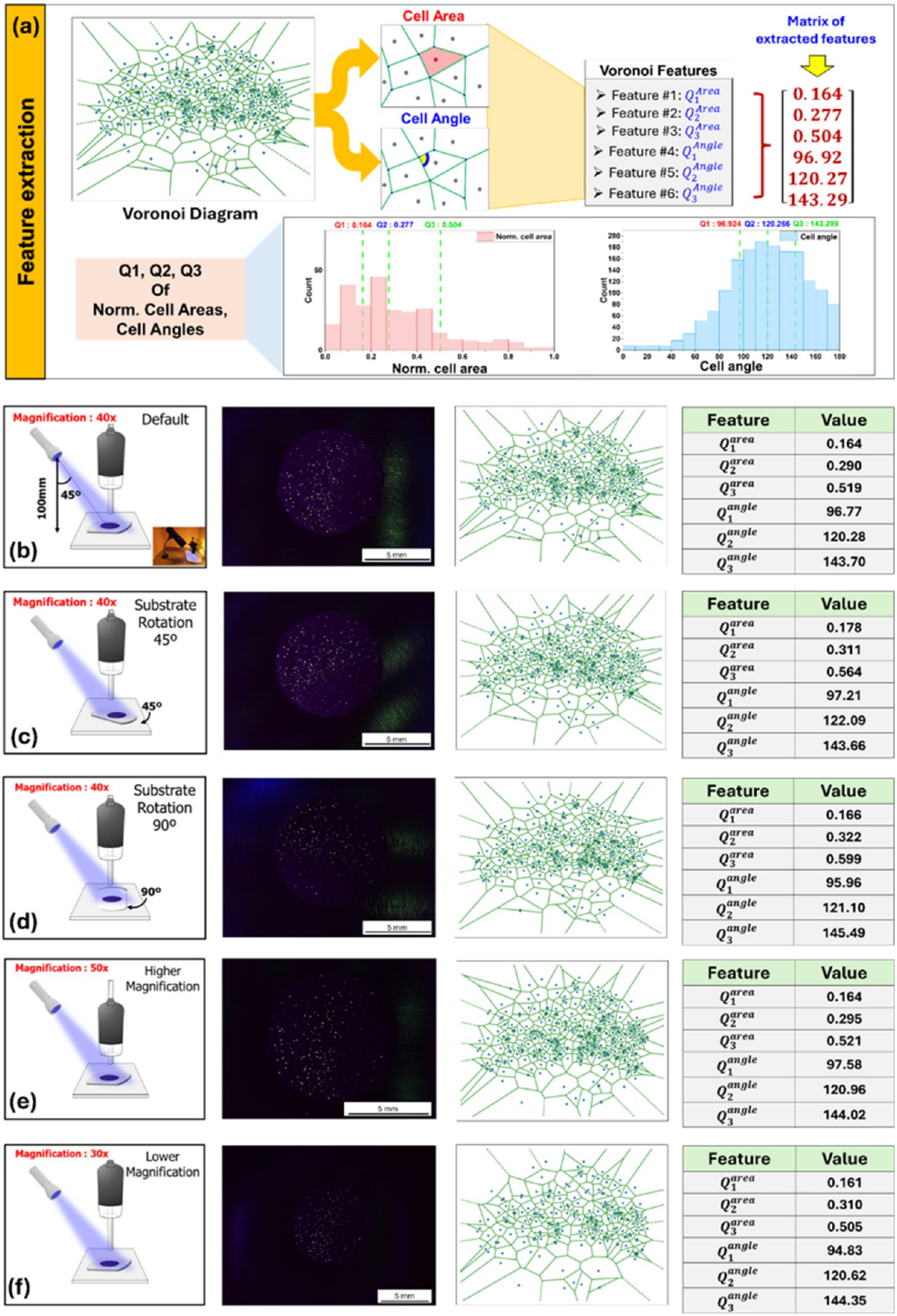

Figure 7. Feature extraction and sensitivity analyses under various image-capturing conditions: (a) Voronoi tessellation for feature extractions. (b) Default condition (baseline) for sensitivity analysis. (c–f) Introduced variations in examinations, along with the corresponding Voronoi diagrams and extracted features for each case.

https://doi.org/10.1021/acsami.5c17570
ACS Appl. Mater. Interfaces XXXX, XXX, XXX−XXX

metrics (i.e., uniformity, intra-HD, and inter-HD) along with the respective advantages and limitations of the fabrication techniques reported in the literature. The results demonstrate that our approach achieves competitive performance while offering a high-throughput, simplified, and scalable fabrication pathway for generating high-entropy unclonable surfaces.

4.2.3. Environmental Exposure and Surface Reliability. To assess the environmental reliability of the fabricated surfaces, a series of durability tests were performed, including thermal cycling, chemical resistance evaluations, and UV exposure, followed by the calculation of uniformity and HD between pre- and postexperiment metrics for comparison. Each test was conducted on two independent PUF specimens to ensure the reliability of the results. Representative surface images acquired at specific intervals throughout each test are provided in Figure S3 (Supporting Information).

First, to evaluate the robustness against temperature variations, thermal cycling tests were carried out to examine the stability of the surface under repeated heating and cooling conditions. The temperature range was set between 50 and 100 °C, remaining below the melting temperature of the fluorescent particles (~ 110 °C). Each cycle included 10 min hold at both temperature limits, with a total of 20 cycles conducted using a programmable oven (*Fusion 17, Paragon Industries*). As shown in Figure 6d, no significant change in uniformity was observed, indicating that the fabricated surfaces exhibit excellent thermal stability within the tested temperature range. The HD results in Figure 6d also verified that the authentication capability remained within an acceptable range.

Next, chemical durability was evaluated by sequentially submerging each sample in salt, acid, and alkali solutions for 12 h each. The test solutions were an alcohol solution saturated with calcium chlorate ($CaCl_2$), pure acetic acid (CH_3COOH), and an aqueous solution saturated with sodium bicarbonate ($NaHCO_3$).[54] The uniformity was measured every 12 h over the entire test period, as presented in Figure 6e. During the chemical exposure, neither the uniformity variation nor the postexperiment HD showed notable changes, confirming the strong resistance of fabricated surfaces to chemical degradation.

Last, the UV exposure tests were conducted under high-density UV illumination to evaluate fluorescence degradation (i.e., also known as fluorophore bleaching[27]). The tests were performed inside a UV dark cabinet (*UV analyzer, Maisutseb*) equipped with four 8 W UV lamps (two at 254 nm and two at 365 nm). The samples were continuously exposed for 3 days, and surface uniformity was measured daily. As shown in Figure 6f, the uniformity exhibited a noticeable decline with an accelerated rate of degradation after the first day of exposure. Furthermore, the HD between pre and post UV exposure confirmed degradation of authentication ability, consistent with fluorophore bleaching being the primary degradation mechanism under UV illumination.[27,56] Taken together, the fabricated surfaces exhibited strong durability against thermal cycling and chemical exposure, although they had a tendency to degrade under prolonged and intense UV illumination. Notably, the bleaching issue can be mitigated by selecting UV-resistant fluorescent sphere materials for use in the CS process.

4.3. Feature Extraction and Sensitivity Analysis

This section describes the methodology used to extract geometric features from as-deposited CS surfaces for PUF generation. The workflow begins with identifying the centroids of fluorescent particles followed by Voronoi tessellation to capture local geometric relationships within the deposition. Geometric descriptors are then extracted from the tessellated structure and evaluated through a sensitivity analysis to assess the robustness. Conventional image feature extraction methods, such as scale-invariant feature transform (SIFT),[57] are unsuitable for this application because the fluorescent patterns consist of randomly distributed particles with highly similar sizes, shapes, and intensities, leading to unstable keypoint detection (see Figure S4, Supporting Information). As such, Voronoi analysis was adopted as an alternative approach due to its effectiveness in representing local spatial relationships. Recognizing that Voronoi tessellation is sensitive to image quality and segmentation accuracy, a dedicated sensitivity analysis was performed using repeated imaging of identical surfaces under varied acquisition conditions.

4.3.1. Voronoi Tessellation. The unique features from the binarized images were generated using Voronoi analysis (tessellation),[58] which divides a plane into distinct cells (regions) based on the proximity of a given point.[6] The resulting partition is termed a Voronoi diagram consisting of polygonal cells (see Figure 7a) generated from a set of K distinct points corresponding to the spatial locations of fluorescent particles on the 2D surface. The Voronoi cell $V_k(i)$ of site k_i (fluorescent particles) is defined as (eq 1)[6,59]

$$V_k(i) = \{q \in \mathbb{R}^2 \mid \|q - k_i\| \leq \|q - k_j\|,\ \forall\, j \neq i,\ k_j \in K\} \tag{1}$$

where $q \in \mathbb{R}^2$ denotes an arbitrary point in the 2D space, k_i is the coordinate of the seed point (i.e., fluorescent particle location for the present study) whose cell is being defined, $k_j \in K$ represents the other sites in the set K (i.e., the coordinates of all fluorescent particles on the surface), and $\|q - k_i\|$ is the Euclidean distance between q and k_i. Accordingly, the Voronoi analysis in this work partitions the surface into regions closest to each fluorescent particle, producing distinct cells that define the spatial domain of each particle.

By its inherent nature, the Voronoi diagram encodes various geometrical properties that facilitate discriminative feature extraction in a spatially adaptive manner.[59] In this study, for the Voronoi analysis, a prenormalization procedure was first applied to the binarized image in order to eliminate inspection-originated variations in location, scale, and orientation[60] (see Figure S5, Supporting Information). This step ensures that extracted features reflect only the spatial arrangement of the fluorescent particle centroids, thereby minimizing imaging inconsistencies. Subsequently, the normalized spatial coordinates of the fluorescent particles were used as the input (i.e., Voronoi seed) for Voronoi tessellation, which partitions the space into distinct cells. This partitioning leads to the formation of the Voronoi diagram as shown in Figure 7a that enables the quantification of local spatial relationships (viz., the cell size, the number of edges, the angle of vertices, etc.), which can be leveraged to encode the characteristics of the as-deposited surface.

In this work, six distinct features were identified to generate PUFs from the as-deposited surface, namely, the 25th, 50th, and 75th quartiles (Q_1, Q_2, Q_3) of the normalized cell areas, together with the corresponding quartile of global cell angles, as shown in Figure 7a (i.e., Q_1^{Area}, Q_2^{Area}, Q_3^{Area}, Q_1^{Angle}, Q_2^{Angle}, and Q_3^{Angle}). Representative illustration of the "cell area" and "cell angle" are presented in the Voronoi diagram in Figure 7a,

https://doi.org/10.1021/acsami.5c17570
ACS Appl. Mater. Interfaces XXXX, XXX, XXX−XXX

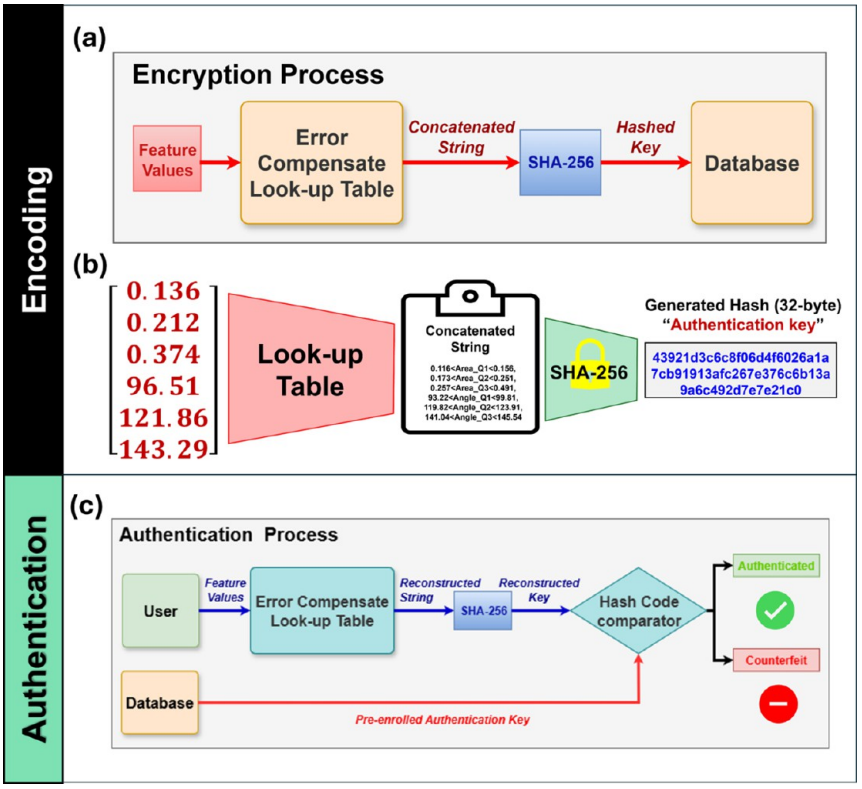

Figure 8. Encryption and authentication process of the as-CS deposited surface: (a) Schematic of the surface encryption process. (b) Encryption of the extracted features using the SHA-256 cryptographic algorithm. (c) Authentication process.

along with the corresponding calculation details provided in Figure S6 (Supporting Information). In detail, the percentile values capture the geometric distribution patterns of the cells in which Q_1 captures the lower tail of the distribution. Q_2 captures the central tendency, and Q_3 captures the upper tail. The normalized cell area quantifies the relative size of each Voronoi cell with respect to the overall mean cell area [i.e., area/(mean area)]. Together, these area- and angle-based metrics are resistant to noise compared to using single extremes (e.g., minimum or maximum cell area), thereby enabling a robust numerical fingerprint of the surface for unique PUF generation. Note that although various features can be extracted from the Voronoi diagram (viz., maximum and minimum Euclidean distances, number of fluorescent particles, etc.), the selected features (i.e., Q_1^{Area}, Q_2^{Area}, Q_3^{Area}, Q_1^{Angle}, Q_2^{Angle}, and Q_3^{Angle}) exhibit higher discriminative capability, making them more effective for uniquely characterizing the fabricated PUFs.

4.3.2. Sensitivity Analysis. Sensitivity analyses of the feature extraction process were conducted under various image-capturing scenarios by introducing potential human- and equipment-induced error sources. As shown in Figure 7b–f, these variations include the substrate orientation and focal distance. While most of these variations can be mitigated during the prenormalization procedure of the Voronoi tessellation, some residual effects may persist due to the sensitivity and inherent limitations of operator- and equipment-dependent optical observations.

To evaluate the sensitivity of the image-capturing process on feature extraction, the baseline measurement conditions, shown in Figure 7b, were defined as a magnification of 40× and a substrate orientation along the x-direction (0°). The performance of various image-capturing scenarios, as illustrated in Figure 7c–f, (i.e., substrate orientation (45°, 90° counterclockwise) and focal distance (30× and 50× magnification)), was evaluated against the default settings in Figure 7b. Subsequently, the features of the Voronoi diagram were extracted for each of the altered cases. The results confirmed that the extracted feature values remained largely consistent across all tested scenarios [i.e., error for each feature: 1.94% for Q_1^{Area}, 6.3% for Q_2^{Area}, 5.16% for Q_3^{Area}, and 0.38% for Q_1^{Angle}, 0.75% for Q_2^{Angle}, and 0.47% for Q_3^{Angle} (see Figure 7b–f, right panels)]. Although the error margins for Q_1^{Area} and Q_2^{Area} were higher than those of the other features, all features remained within the 10% error margin. Accordingly, we retained the full feature set for encoding and hashing in the subsequent sections to ensure the transparency and completeness of the analysis. In practice, however, if any feature were to exceed the acceptable threshold, it could be excluded during preprocessing by omitting that feature index across all collected samples prior to encoding. For instance, the high-error quartiles (Q_1^{Area} and Q_2^{Area}) could be omitted, while the low-error quartiles (i.e., Q_3^{Area}, Q_1^{Angle}, Q_1^{Area}, and Q_2^{Area}) could be retained to construct a more robust feature matrix for encoding and hashing. Collectively, the sensitivity analysis confirmed the robustness of the feature extraction process against variations in image quality and image-capturing conditions.

4.4. Surface Encryption

For robust encryption of the fabricated surfaces, the allowable tolerance window (error limits) for the extracted feature values must be empirically determined. A tolerance that is too narrow may cause frequent misidentification due to optical measurement errors, while one that is too broad compromises authentication by failing to distinguish genuine from counter-

https://doi.org/10.1021/acsami.5c17570
ACS Appl. Mater. Interfaces XXXX, XXX, XXX−XXX

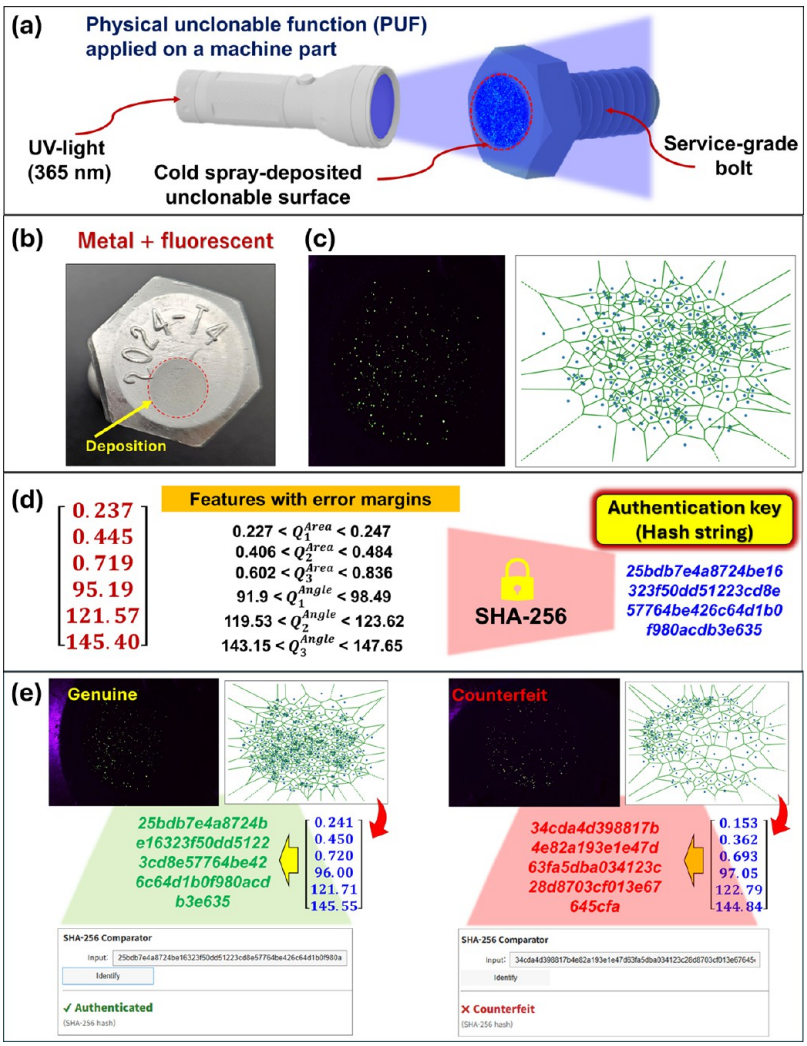

Figure 9. Case study of part authentication: (a) Illustration of PUF application on a service-grade bolt. (b) Surface deposition using metal + fluorescent powder blend. (c) Microscope images under UV light exposure and corresponding Voronoi diagrams. (d) Encryption of the deposited surface. (e) Demonstration of authentication.

feit items. Based on the sensitivity evaluations in Section 4.3.2, first, we quantified the error range for each feature and compiled these bounds into a practical lookup table to guide the construction of resilient authentication keys (see Figure S7, Supporting Information). This approach accounts for measurement errors and normalizes the boundaries, thereby ensuring robust and reliable encryption and authentication. Although the lookup table is generated for each PUF sample, the error tolerance derived from the Voronoi tessellation is applied across all encryption and verification processes, thereby substantially reducing computational complexity.

Next, using the extracted feature values (Figure 7a) together with the lookup table (Table S2, Supporting Information), a concatenated string is generated (e.g., "0.116 ≤ Q_1^{Area} < 0.156, ..."), accounting for all features and their respective error margins (Figure 8a,b). Herein, the concatenated string represents a global string that integrates all of the features along with their associated error margins. This global string not only preserves the uniqueness of each feature but also incorporates tolerance for measurement variability.

Lastly, as shown in Figure 8b, the constructed concatenated string is hashed using the SHA-256 cryptographic algorithm[61] to generate the "authentication key." SHA-256 is a widely accepted cryptographic hash function that maps an arbitrary-length input to a fixed 256-bit message digest.[62] The resulting hash exhibits strong one-way and tamper-resistant properties, ensuring that even a single-bit variation in the input string produces a substantially different output. This characteristic is particularly advantageous for PUFs as it guarantees both uniqueness and unpredictability of the generated authentication keys while providing resistance against reverse engineering or counterfeit attempts.

4.5. Surface Authentication

To authenticate the surface, the authentication key (i.e., 256-bit cryptographic hash) must be regenerated in the verification phase by following steps 1−3 outlined in Figure 2 (see blue arrows). Once the features are encrypted and the hash is obtained (Figure 8a), the generated hash is subsequently compared to the reference hash created during the enrollment phase, as illustrated in Figure 8c. A successful match validates the authenticity of the surface, while any mismatch indicates potential tampering or counterfeit attempts. This verification workflow ensures a robust, repeatable, and tamper-evident authentication mechanism for CS-fabricated surfaces.

https://doi.org/10.1021/acsami.5c17570
ACS Appl. Mater. Interfaces XXXX, XXX, XXX−XXX

5. CASE STUDY ON PART AUTHENTICATION

To demonstrate and validate the proposed manufacturing pathway together with its complementary authentication pipeline, a case study was conducted by depositing surfaces on the service-grade bolts (*Aluminum 2024-T4 Heavy Hex Bolt*), as illustrated in Figure 9a. The surfaces were successfully fabricated (Figure 9b), and subsequent optical imaging combined with Voronoi analysis enabled the digitization of the surface (Figure 9c). The unique features were then extracted from the Voronoi diagram, accounting for potential measurement-induced errors, and subsequently encoded using the SHA-256 algorithm to generate the authentication key (Figure 9d), which was then stored in a database. Last, the generated PUF on the bolt structure underwent authentication testing following the verification process in Figure 2.

Figure 9e shows the deposited surfaces and their corresponding Voronoi diagrams for two bolts: one treated as a genuine bolt (Figure 9e, left panel and Figure S8a, Supporting Information) and the other as a counterfeit part (Figure 9e, right panel, and Figure S8b, Supporting Information). The key generated during verification (Figure 9d) was then compared to the corresponding authentication key stored in the database. As presented in Figure 9e, the framework demonstrated strong resilience in authenticating the correct part while rejecting the nonmatching key during cross-sample comparisons, thereby minimizing false positives and ensuring high authentication reliability.

In addition to the metal−fluorescent blend feedstock, we also tested CS deposition using fluorescent particles alone to achieve fully hidden PUFs. As shown in Figure 10a, the fluorescent particles were successfully deposited on the bolt, and the surface enrollment process was subsequently applied, as illustrated in Figure 10b,c. However, unlike the fluorescent−metal mixture, the adhesion strength of the fluorescent powder-only coating exhibited poor adhesion to the substrate, resulting in localized removal during Scotch tape tests (Figure S9a, Supporting Information). This observation indicates that blending fluorescent microspheres with metal powders enhances coating adhesion by promoting mechanical interlocking and improving particle−substrate bonding (see SEM images in Figure 4). On the one hand, surface pretreatment of the bolt via sandblasting (120-grit aluminum oxide) prior to CS enhanced the interfacial adhesion strength between the fluorescent powders and the bolt substrate, resulting in more durable fluorescent coatings (see Figure S9b, Supporting Information). Overall, the results suggest that controlled abrasive blasting can enable fluorescent powder-only deposition by promoting particle embedment and interlocking, thus allowing fully invisible optical PUFs on mechanical components.

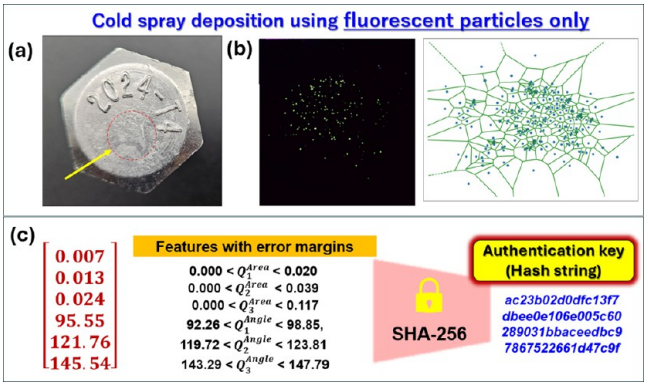

Figure 10. CS deposition using fluorescent particles only: (a) CS-deposited bolt surface. (b) Corresponding microscope image (left) and Voronoi diagram (right). (c) Surface feature extraction and enrollment process.

Besides, we evaluated the proposed CS-based manufacturing approach across various material systems, including metals (i.e., aluminum, copper) and polymers [i.e., polylactic acid and polyethylene terephthalate (PET)]. In all cases, the results validated the feasibility of CS-based unclonable surface fabrication using fluorescent powders alone (see Figure S10, Supporting Information). Particularly, the demonstrated feasibility on Cu and PET could make the proposed approach viable for both rigid and flexible electronics applications as these materials are widely used in electronic devices.[63]

6. DISCUSSION

Unlike conventional manufacturing methods that prioritize repeatability, the CS process inherently introduces randomness, producing physically unclonable surfaces. When digitized into surface fingerprints, these features provide a strong resistance to counterfeiting. Furthermore, by coupling material-level stochasticity with cryptographic reinforcement, CS-based PUFs offer a robust pathway for secure authentication against counterfeiting in critical sectors. Nevertheless, the developed framework may pose several challenges, as outlined below:

i. *Surface topology*: Given that CS relies on the metallurgical bonding of sprayed particles with the underlying substrate, it locally alters the topology of the as-deposited surface (see Figure 9b). This may limit the applicability of the proposed approach to cases involving sensitive substrates or components where surface integrity, dimensional tolerance, or functional performance must be strictly preserved.

ii. *Feature extraction*: To reduce equipment- or operator-induced variability, surface features were extracted from quartiles of the Voronoi cell angles and areas (i.e., Q_1−Q_3, Figure 7a). With large sample sets, these quartiles may converge to overlapping intervals, increasing the risk of false positives. As an alternative, discrete features (e.g., Euclidean distances, particle count, and vertex angles) can be derived from the spatial distribution of fluorescent particles to better distinguish deposited surfaces (Figure S11, Supporting Information). This approach, however, involves a trade-off as larger measurement error margins may increase the likelihood of false negatives during authentication. Therefore, advanced error-correction strategies and robust feature extraction methods are critical to minimize deviations and ensure reliable surface authentication.

iii. *Environmental stressors*: Even though the fabricated surfaces demonstrated promising durability against environmental stressors such as thermal cycling and chemical exposure, long-term durability assessments are essential to validate the reliability of CS-based PUFs, particularly with respect to wear and corrosion resistance.

https://doi.org/10.1021/acsami.5c17570
ACS Appl. Mater. Interfaces XXXX, XXX, XXX−XXX

7. CONCLUSIONS

This work introduced an innovative approach for fabricating physically unclonable surfaces using the CS technique, which leverages its inherently stochastic turbulent two-phase flow to embed hidden optical features onto the target surface in a single step. The approach is further complemented by algorithmic feature extraction and cryptographic surface encoding, enabling the generation of robust and resilient PUFs for smart part authentication. Based on the results, the following conclusions can be drawn:

- The optical fluorescent powders were directly deposited in a single step, achieving strong adhesion strength and ensuring stable integration with the substrate.
- The fabricated surfaces exhibited strong uniqueness, characterized by a mean uniformity of 0.507, an inter-HD of 0.481, and an intra-HD of 0.068, thereby confirming the distinctiveness of the surfaces. Furthermore, the benchmarking analysis (Table 1) showed that the proposed CS-based PUFs offer promising uniqueness and reliability, along with process simplicity and scalability.
- The surfaces demonstrated strong durability under thermal and chemical stresses, showing no significant degradation of uniqueness, as confirmed by the PUF metrics (i.e., average HDs of 0.186 and 0.211, respectively). In contrast, noticeable degradation occurred under UV exposure due to photobleaching.
- The developed image-processing and feature-extraction pipeline produced distinct surface features with minimal sensitivity (i.e., 0.38−6.3%) to equipment- or operator-induced errors.
- The cryptographic encoding of the extracted features demonstrated strong robustness and resilience against counterfeiting, ensuring secure and reliable authentication, with an FPR of 2.05×10^{-10} and a cloning probability of 4.73×10^{-7}.
- The proposed CS-based PUF manufacturing pathway demonstrated feasibility across diverse material systems (i.e., from metals to polymers).

Future work may focus on evaluating the long-term durability of the fabricated PUFs under various environmental stressors. In addition, exploring machine learning-assisted feature extraction offers a promising pathway to enhance robustness and improve tamper evidence.

ASSOCIATED CONTENT

Supporting Information

The Supporting Information is available free of charge at https://pubs.acs.org/doi/10.1021/acsami.5c17570.

Adhesion tests for the as-CS surfaces using metal−fluorescent powder blend; surface uniqueness evaluation via uniformity, inter-HD, and intra-HD metrics; environmental durability tests of the as-deposited surfaces; keypoint matching in SIFT-based feature extraction; normalization procedure of the point-coordinate data; feature extraction procedure from the Voronoi diagram; sensitivity evaluation data and error compensation procedure; case study: PUF-enabled part authentication; scotch tape test of the as-CS surfaces; feasibility of the proposed manufacturing approach across different material systems; feature extraction from as-cold-sprayed surfaces; NIST 800-22 randomness test results; and lookup table for physically unclonable surface authentication (PDF)

Real-time video of CS surface deposition (MP4)

Scotch-tape adhesion tests (MP4)

AUTHOR INFORMATION

Corresponding Author

Semih Akin − *Department of Mechanical, Aerospace and Nuclear Engineering and Center for Smart Convergent Manufacturing Systems (CSCMS), Rensselaer Polytechnic Institute, Troy, New York 12180, United States;* orcid.org/0000-0002-3644-7133; Email: akins@rpi.edu

Author

Jaehun Jeon − *Department of Mechanical, Aerospace and Nuclear Engineering, Rensselaer Polytechnic Institute, Troy, New York 12180, United States*

Complete contact information is available at: https://pubs.acs.org/10.1021/acsami.5c17570

Author Contributions

J.J.: Conceptualization, methodology, formal analysis, investigation, design, experiments, characterization, and writing original draft. S.A.: Conceptualization, methodology, formal analysis, investigation, supervision, resources, and writing-review and editing.

Notes

The authors declare the following competing financial interest(s): The authors have a patent pending on this topic through Rensselaer Polytechnic Institute (RPI).

ACKNOWLEDGMENTS

The authors acknowledge the internal funding provided by the Department of Mechanical, Aerospace, and Nuclear Engineering (MANE) at Rensselaer Polytechnic Institute (RPI).

REFERENCES

(1) Gao, R. X.; Krüger, J.; Merklein, M.; Möhring, H.-C.; Váncza, J. Artificial Intelligence in manufacturing: State of the art, perspectives, and future directions. *CIRP Annals* **2024**, *73*, 723−749.

(2) Kotzé, J.; Antonopoulos, G. A. Con Air: exploring the trade in counterfeit and unapproved aircraft parts. *British Journal of Criminology* **2023**, *63*, 1293−1308.

(3) Porter, W.; Reese, C.; Bickford, J.; Bourn, S.; Van Bossuyt, D. L. The impact of counterfeit components and LRUs in the navy surface warfare supply chain: A systems dynamics approach. *Systems Engineering* **2025**, *28*, 157−174.

(4) Mura, G. Counterfeit electronics: a threat for new space economy. In *Small Satellites Systems and Services Symposium (4S 2024)*; SPIE: 2025; pp 1751−1757.

(5) Friedman, J.; Ciccarone, D. The public health risks of counterfeit pills. *Lancet Public Health* **2025**, *10*, e58−e62.

(6) Agrawal, T. K.; Koehl, L.; Campagne, C. A secured tag for implementation of traceability in textile and clothing supply chain. *International Journal of Advanced Manufacturing Technology* **2018**, *99*, 2563−2577.

(7) Shen, A.; Turner, S.; Antonopoulos, G. Driven to Death: A Chinese case study on the counterfeiting of automotive components. *Asian Journal of Criminology* **2022**, *17*, 311−329.

(8) Sullivan, B. A.; Wilson, J. M. An empirical examination of product counterfeiting crime impacting the US military. *Trends in Organized Crime* **2017**, *20*, 316−337.

(9) Lewis, K. The fake and the fatal: The consequences of counterfeits. *Park Place Econ.* **2009**, *17*, 14.
(10) OECD. European Union Intellectual Property Office (EUIPO). In *Mapping Global Trade in Fakes 2025: Global Trends and Enforcement Challenges*; OECD: **2025**.
(11) Organisation for Economic Co-operation and Development (OECD). *Global trade in fake goods reached USD 467 billion, posing risks to consumer safety and compromising intellectual property*. Press release, **2025**.
(12) Park, I.-Y.; Ahn, S.; Kim, Y.; Bae, H.-S.; Kang, H.-S.; Yoo, J.; Noh, J. Serial number coding and decoding by laser interference direct patterning on the original product surface for anti-counterfeiting. *Opt. Express* **2017**, *25*, 14644−14653.
(13) Shankar, B. P.; Rajkumar, N.; Viji, C.; Kumar, K. D.; Saravanakumar, S.; Mohanraj, A. Approach to Identifying Counterfeit Products with QR Codes and Computational Algorithms. In *2024 5th International Conference on Smart Electronics and Communication (ICOSEC)*; IEEE: 2024; pp 1203−1209.
(14) Jeon, H.-J.; Leem, J. W.; Ji, Y.; Park, S. M.; Park, J.; Kim, K.-Y.; Kim, S.-W.; Kim, Y. L. Cyber-physical watermarking with inkjet edible bioprinting. *Adv. Funct. Mater.* **2022**, *32*, No. 2112479.
(15) Gomes, H.; Navio, F.; Gaspar, P. D.; Soares, V. N.; Caldeira, J. M. Radio-frequency identification traceability system implementation in the packaging section of an industrial company. *Applied Sciences* **2023**, *13*, 12943.
(16) Kumar, V.; Das, S. K. Enhancing security in IIoT: RFID authentication protocol for edge computing and blockchain-enabled supply chain. *Cyber Security and Applications* **2025**, *3*, No. 100087.
(17) Tsai, K.-Y.; Wei, Y.-L.; Chi, P.-S. Lightweight privacy-protection RFID protocol for IoT environment. *Internet of Things* **2025**, *30*, No. 101490.
(18) Wu, H.; Wang, S.; Pu, C.; Ma, J.; Zeng, Y. Enhancing counterfeit RFID tag classification through distance based cognitive risk control. *Sci. Rep.* **2025**, *15*, 4150.
(19) Vidal, N.; Lopez-Villegas, J. M.; Romeu, J.; Barenys, A. S.; Garcia-Miquel, A.; González-López, G.; Jofre, L. 3D-printed UHF-RFID tag for embedded applications. *IEEE access* **2020**, *8*, 146640−146647.
(20) Schmitz, T.; Costa, L.; Canfield, B. K.; Kincaid, J.; Zameroski, R.; Garcia, R.; Frederick, C.; Rossy, A. M.; Moeller, T. M. Embedded QR code for part authentication in additive friction stir deposition. *Manufacturing Letters* **2023**, *35*, 16−19.
(21) Zahoor, F.; Bature, U. I.; Nisar, A.; Alzahrani, A.; Abbas, H.; Bashir, F. A Comprehensive Review on Physical Unclonable Functions Based on Resistive Random Access Memory. *ACS Applied Electronic Materials* **2025**, *7*, 6215−6242.
(22) Kim, C.; Son, S.; Park, Y. A Privacy-Preserving Authentication Scheme Using PUF and Biometrics for IoT-Enabled Smart Cities. *Electronics* **2025**, *14*, 1953.
(23) Al-Meer, A.; Al-Kuwari, S. Physical unclonable functions (PUF) for IoT devices. *ACM Computing Surveys* **2023**, *55*, 1−31.
(24) Klausen, M.; Zhang, J.; Stevens, M. M. Designing Physical Unclonable Functions From Optically Active Materials. *Adv. Mater.* **2025**, *37*, No. 2502059.
(25) Sandomirskii, M.; Petrova, E.; Kustov, P.; Chizhov, L.; Larin, A.; Bruyère, S.; Yaroshenko, V.; Ageev, E.; Belov, P.; Zuev, D. Spectral physical unclonable functions: downscaling randomness with multi-resonant hybrid particles. *Nat. Commun.* **2025**, *16*, 5097.
(26) Torun, N.; Torun, I.; Sakir, M.; Kalay, M.; Onses, M. S. Physically unclonable surfaces via dewetting of polymer thin films. *ACS Appl. Mater. Interfaces* **2021**, *13*, 11247−11259.
(27) Mann-Andrews, E.; McGrath, T.; Halliday, B.; Young, R. J. A guide for assessing optically imaged physically unclonable functions for authentication. *Appl. Phys. Rev.* **2025**, *12*, No. 021314.
(28) Li, T.; Guo, X.; Müller, F.; Abdulazhanov, S.; Ma, X.; Zhong, H.; Liu, Y.; Narayanan, V.; Yang, H.; Ni, K.; et al. Demonstration of high-reconfigurability and low-power strong physical unclonable function empowered by FeFET cycle-to-cycle variation and charge-domain computing. *Nat. Commun.* **2025**, *16*, 189.
(29) Park, T.; Kim, J.; Ko, R.; Park, B.; Yoo, H. Light in, sound keys out: photoacoustic PUFs from stochastic nanocomposites. *Nat. Commun.* **2025**, *16*, 7323.
(30) Kehayias, P.; Bussmann, E.; Lu, T.-M.; Mounce, A. M. A physically unclonable function using NV diamond magnetometry and micromagnet arrays. *J. Appl. Phys.* **2020**, *127*, 203904.
(31) Esidir, A.; Pekdemir, S.; Kalay, M.; Onses, M. S. Ultradurable embedded physically unclonable functions. *ACS Appl. Mater. Interfaces* **2024**, *16*, 16532−16543.
(32) Esidir, A.; Kiremitler, N. B.; Kalay, M.; Basturk, A.; Onses, M. S. Unclonable features via electrospraying of bulk polymers. *ACS Applied Polymer Materials* **2022**, *4*, 5952−5964.
(33) Kayaci, N.; Ozdemir, R.; Kalay, M.; Kiremitler, N. B.; Usta, H.; Onses, M. S. Organic light-emitting physically unclonable functions. *Adv. Funct. Mater.* **2022**, *32*, No. 2108675.
(34) Nocentini, S.; Rührmair, U.; Barni, M.; Wiersma, D. S.; Riboli, F. All-optical multilevel physical unclonable functions. *Nature materials* **2024**, *23*, 369−376.
(35) Liu, Y.; Han, F.; Li, F.; Zhao, Y.; Chen, M.; Xu, Z.; Zheng, X.; Hu, H.; Yao, J.; Guo, T.; et al. Inkjet-printed unclonable quantum dot fluorescent anti-counterfeiting labels with artificial intelligence authentication. *Nat. Commun.* **2019**, *10*, 2409.
(36) Kamwe Sighano, S.; Ritacco, T.; Bruno, M. D. L.; Gennari, O.; Fuscaldo, W.; Zografopoulos, D. C.; Marae-Djouda, J.; Maurer, T.; Beccherelli, R.; Caputo, R.; et al. Optical and Terahertz Anti-counterfeiting Tags Via Non-Deterministic Deposition of Fluorescent Opuntia Ficus-Indica Extract. *Adv. Funct. Mater.* **2024**, *34*, No. 2406632.
(37) Li, Y.; Li, Y.; Yang, J.; Chen, Z.; Feng, M.; Liu, L.; Song, F.; Huang, W. Dual Challenge−Response Systems of a Three-Dimensional "Bionic" Fluorescent Physically Unclonable Function Label. *ACS Appl. Mater. Interfaces* **2024**, *16*, 25256−25267.
(38) Akin, S.; Lee, S.; Jo, S.; Ruzgar, D. G.; Subramaniam, K.; Tsai, J.-T.; Jun, M. B.-G. Cold spray-based rapid and scalable production of printed flexible electronics. *Additive Manufacturing* **2022**, *60*, No. 103244.
(39) Wang, Z.; Mao, P.; Huang, C.; Yu, P.; Li, W.; Yin, S. Deposition mechanism of ceramic reinforced metal matrix composites via cold spraying. *Additive Manufacturing* **2024**, *85*, No. 104167.
(40) Tauro, F.; Grimaldi, S.; Petroselli, A.; Porfiri, M. Fluorescent particle tracers for surface flow measurements: A proof of concept in a natural stream. *Water Resour. Res.* **2012**, *48*, No. 011610.
(41) Guo, D.; Kazasidis, M.; Hawkins, A.; Fan, N.; Leclerc, Z.; MacDonald, D.; Nastic, A.; Nikbakht, R.; Ortiz-Fernandez, R.; Rahmati, S.; et al. Cold spray: over 30 years of development toward a hot future. *Journal of thermal spray technology* **2022**, *31*, 866−907.
(42) Champagne, V.; Helfritch, D. The unique abilities of cold spray deposition. *International Materials Reviews* **2016**, *61*, 437−455.
(43) Pattison, J.; Celotto, S.; Khan, A.; O'neill, W. Standoff distance and bow shock phenomena in the Cold Spray process. *Surf. Coat. Technol.* **2008**, *202*, 1443−1454.
(44) Akin, S.; Wu, P.; Tsai, J.-T.; Nath, C.; Chen, J.; Jun, M. B.-G. A study on droplets dispersion and deposition characteristics under supersonic spray flow for nanomaterial coating applications. *Surf. Coat. Technol.* **2021**, *426*, No. 127788.
(45) Gabor, T.; Akin, S.; Jun, M. B.-G. Numerical studies on cold spray gas dynamics and powder flow in circular and rectangular nozzles. *Journal of Manufacturing Processes* **2024**, *114*, 232−246.
(46) Han, C.; Gabor, T.; Lee, H.; Lee, J.; Akin, S.; Jun, M. B.-G. Pulsed Cold Spray System for Physical Unclonable Function Generation. *Procedia CIRP* **2025**, *137*, 176−180.
(47) Gabor, T.; Wang, Y.; Akin, S.; Zhou, F.; Chen, J.; Jeon, Y.; Jun, M. B.-G. Design, modeling, and characterization of a pulsed cold spray system. *Surf. Coat. Technol.* **2025**, *503*, No. 131984.
(48) Nikbakht, R.; Chromik, R.; Jodoin, B. A novel approach for manufacturing cellular metallic structures using pulsed gas dynamic spraying process. *Additive Manufacturing* **2023**, *66*, No. 103473.

https://doi.org/10.1021/acsami.5c17570
ACS Appl. Mater. Interfaces XXXX, XXX, XXX−XXX

(49) Herder, C.; Yu, M.-D.; Koushanfar, F.; Devadas, S. Physical unclonable functions and applications: A tutorial. *Proceedings of the IEEE* **2014**, *102*, 1126−1141.
(50) Jacobs, K. *Discrete Stochastics*; Springer: 1992; pp 65−101.
(51) Bassham, III. L. E.; Rukhin, A. L.; Soto, J.; Nechvatal, J. R.; Smid, M. E.; Barker, E. B.; Leigh, S. D.; Levenson, M.; Vangel, M.; Banks, D. L. et al. *Sp 800−22 rev. 1a. a statistical test suite for random and pseudorandom number generators for cryptographic applications*; NIST: 2010.
(52) Li, X.; Lin, B.; Gao, B.; Lu, Y.; Yang, S.; Su, Z.; Shen, T.-Y.; Tang, J.; Qian, H.; Wu, H. A memristor-based unified PUF and TRNG chip with a concealable ability for advanced edge security. *Sci. Adv.* **2025**, *11*, No. eadr0112.
(53) Kim, M. S.; Lee, G. J.; Leem, J. W.; Choi, S.; Kim, Y. L.; Song, Y. M. Revisiting silk: a lens-free optical physical unclonable function. *Nat. Commun.* **2022**, *13*, 247.
(54) Wang, Z.; Wang, H.; Wang, P.; Shao, Y. Robust optical physical unclonable function based on total internal reflection for portable authentication. *ACS Appl. Mater. Interfaces* **2024**, *16*, 27926−27935.
(55) Qiang, S.; Yuan, K.; Cheng, Y.; Long, G.; Zhang, W.; Lin, X.; Chai, X.; Fang, X.; Ding, T. A multicolor carbon dot doped nanofibrous membrane for unclonable anti-counterfeiting and data encryption. *Journal of Materials Chemistry C* **2023**, *11*, 7076−7087.
(56) Zhang, J.; Creamer, A.; Xie, K.; Tang, J.; Salter, L.; Wojciechowski, J. P.; Stevens, M. M. Bright and stable anti-counterfeiting devices with independent stochastic processes covering multiple length scales. *Nat. Commun.* **2025**, *16*, 502.
(57) Burger, W.; Burge, M. J. *Digital Image Processing: An Algorithmic Introduction*; Springer: 2022; pp 709−763.
(58) Aurenhammer, F. Voronoi diagrams—a survey of a fundamental geometric data structure. *ACM computing surveys (CSUR)* **1991**, *23*, 345−405.
(59) Okabe, A.; Boots, B.; Sugihara, K.; Chiu, S. N. *Spatial tessellations: concepts and applications of Voronoi diagrams*; John and Wiley: 2009.
(60) Paquet, E.; Rioux, M.; Murching, A.; Naveen, T.; Tabatabai, A. Description of shape information for 2-D and 3-D objects. *Signal Process.: Image Commun.* **2000**, *16*, 103−122.
(61) Brandman, J.; Sturm, L.; White, J.; Williams, C. A physical hash for preventing and detecting cyber-physical attacks in additive manufacturing systems. *Journal of Manufacturing Systems* **2020**, *56*, 202−212.
(62) Paar, C.; Pelzl, J. *Understanding cryptography*; Springer: 2010; Vol. *1*.
(63) Nair, N. M.; Zumeit, A.; Dahiya, R. Transparent and Transient Flexible Electronics. *Adv. Sci.* **2025**, *12*, No. e05133.

https://doi.org/10.1021/acsami.5c17570
ACS Appl. Mater. Interfaces XXXX, XXX, XXX−XXX